

1 Simulating CO<sub>2</sub> profiles using NIES TM and comparison with  
2 HIAPER Pole-to-Pole Observations

3

4 Ci Song<sup>1,2</sup>, Shamil Maksyutov<sup>3</sup>, Dmitry Belikov<sup>3,4,5</sup>, Hiroshi Takagi<sup>3</sup>, and  
5 Jiong Shu<sup>1</sup>

6 [1]Key Laboratory of Geographic Information Science, Institute of Climate Change,  
7 East China Normal University, Shanghai 200241, China

8 [2]College of Science, Zhongyuan University of Technology, Henan, China

9 [3]National Institute for Environmental Studies, Tsukuba 305-8506, Japan

10 [4] National Institute of Polar Research, Tokyo, Japan

11 [5] Tomsk State University, Tomsk, Russia

12 Correspondence to: S. Jiong ( [jshu@geo.ecnu.edu.cn](mailto:jshu@geo.ecnu.edu.cn) )

13

14 **Abstract.** We present a study on validation of the National Institute for Environmental  
15 Studies Transport Model (NIES TM) by comparing to observed vertical profiles of  
16 atmospheric CO<sub>2</sub>. The model uses a hybrid sigma-isentropic ( $\sigma$ - $\theta$ ) vertical coordinate  
17 that employs both terrain-following and isentropic parts switched smoothly in the  
18 stratosphere. The model transport is driven by reanalyzed meteorological fields and  
19 designed to simulate seasonal and diurnal cycles, synoptic variations, and spatial  
20 distributions of atmospheric chemical constituents in the troposphere. The model  
21 simulations were run for **combination of** biosphere, fossil fuel, air-ocean exchange,  
22 biomass burning and inverse correction fluxes of carbon dioxide (CO<sub>2</sub>) by GOSAT

23 Level 4 product. We compared the NIES TM simulated fluxes with data from the  
24 HIAPER Pole-to-Pole Observations (HIPPO) Merged 10-second Meteorology,  
25 Atmospheric Chemistry, and Aerosol Data, including HIPPO-1, HIPPO-2 and  
26 HIPPO-3 from 128.0E to -84.0W, and 87.0N to -67.2S.

27 The simulation results were compared with CO<sub>2</sub> observations made in January and  
28 November, 2009, and March and April, 2010. The analysis attests that the model is  
29 good enough to simulate vertical profiles with errors generally within 1–2 ppmv, except  
30 for the lower stratosphere in the Northern Hemisphere high latitudes.

## 31 **1 Introduction**

32 Atmospheric carbon dioxide (CO<sub>2</sub>) is the primary radiative forcing greenhouse gas  
33 produced by human activities. It causes the most global warming (IPCC, 2013) and its  
34 atmospheric concentration has been increasing at a progressively faster rate each decade  
35 because of rising global emissions (Raupach et al., 2007). The monitoring of  
36 atmospheric CO<sub>2</sub> from space is intended to identify the sources and sinks of the  
37 greenhouse gases generated by human and natural activities. A number of satellites are  
38 actively monitoring greenhouse gases (e.g., GOSAT, SCIAMACHY, AIRS, IASI) to  
39 answer this question, and retrieval algorithms for CO<sub>2</sub> have been developed for these  
40 satellite observation data to provide more accurate estimates of CO<sub>2</sub> concentrations  
41 using several different methods.

42 The sparseness and spatial inhomogeneity of the existing surface network have  
43 limited our ability to understand the quantity and spatiotemporal distribution of CO<sub>2</sub>  
44 sources and sinks (Scholes et al., 2009). Recent studies of global sources and sinks of

45 greenhouse gases, and their concentrations and distributions, have been mainly based  
46 on in situ surface measurements (GLOBALVIEW-CO<sub>2</sub>, 2010). The diurnal and  
47 seasonal “rectifier effect”, the covariance between surface fluxes and the strength of  
48 vertical mixing, and the proximity of local sources and sinks to surface measurement  
49 sites all have an influence on the measured and simulated concentrations, and  
50 complicate the interpretation of results (Denning et al., 1996; Gurney et al., 2004; Baker  
51 et al., 2006). Comparatively speaking, the vertical integration of mixing ratio divided  
52 by surface pressure, denoted as the column-averaged dry-air mole fraction (DMF;  
53 denoted XG for gas G) is much less sensitive to the vertical redistribution of the tracer  
54 within the atmospheric column (e.g., due to variations in planetary boundary layer (PBL)  
55 height) and is more easily related to the underpinning surface fluxes than are near-  
56 surface concentrations (Yang et al., 2007). Thus, column-averaged measurements and  
57 simulations are expected to be very useful for improving our understanding of the  
58 carbon cycle (Yang et al., 2007; Keppel-Aleks et al., 2011; Wunch et al., 2011). In  
59 addition, atmospheric transport has to be accounted for when analyzing the  
60 relationships between observations of atmospheric constituents and their sources/sinks  
61 near the earth’s surface or through the chemical transformation in the atmosphere. As  
62 a result, reliable estimates of climate change depend upon our ability to predict  
63 atmospheric CO<sub>2</sub> concentrations, which requires further investigation of the CO<sub>2</sub>  
64 sources, sinks, and atmospheric transport.

65 Global atmospheric tracer transport models are usually applied to studies of the  
66 global cycles of the long-lived atmospheric trace gases, such as CO<sub>2</sub> and methane (CH<sub>4</sub>),

67 because the long-lived atmospheric tracers exhibit observable global patterns (e.g., the  
68 interhemispheric gradient of the concentration). Global three-dimensional chemistry  
69 transport models (hereafter referred to as CTMs), driven by actual meteorology from  
70 numerical weather predictions, and global circulation models (GCMs) play a crucial  
71 role in assessing and predicting change in the composition of the atmosphere due to  
72 anthropogenic activities and natural processes (Rasch et al., 1995; Jacob et al., 1997;  
73 Denning et al., 1999; Bregman et al., 2006; Law et al., 2008; Maksyutov et al., 2008;  
74 Patra et al., 2008).

75 The transport modeling is done on different scales ranging from local plume spread,  
76 regional mesoscale transport to global scale analysis, depending on the scale of the  
77 phenomena that are studied. Forward modeling is used to estimate tracer concentrations  
78 in regions that lack observation data and to identify the features of tracer transport and  
79 dispersion (Law et al., 2008; Patra et al., 2008). Inverse methods are generally applied  
80 when interpreting the data, with atmospheric transport models providing the link  
81 between surface gas fluxes and their subsequent influence on atmospheric  
82 concentrations (Rayner and O'Brien, 2001; Patra et al., 2003a,b; Gurney et al., 2004;  
83 Baker et al., 2006). Global modeling analysis has helped to identify the relative  
84 contribution of the land and oceans in the Northern and Southern hemispheres to the  
85 interhemispheric concentration differences in CO<sub>2</sub>, CH<sub>4</sub>, carbon monoxide (CO) and  
86 other tracer species (Bolin and Keeling, 1963; Hein et al., 1997). For stable and slowly  
87 reacting chemical species, a number of studies have derived information on the spatial  
88 and temporal distribution of the surface sources and sinks by applying a transport model

89 and atmospheric observations (Tans et al., 1990; Rayner et al., 1999).

90 There are several factors that strongly influence model performance: the numerical  
91 transport algorithm used, meteorological data, grid type and resolution. In tracer  
92 transport calculations, semi-Lagrangian transport algorithms are often used in  
93 combination with finite-volume models. Losses in the total tracer mass are possible in  
94 these algorithms. While such losses are often negligible for short-term transport  
95 simulations, they can seriously distort the global trends and tracer budgets in long-term  
96 simulations. To avoid such losses, various mass-fixing schemes have been applied  
97 (Hack et al., 1993; Rasch et al., 1995). Although the use of mass fixers can prevent  
98 mass losses, there remains a possibility of predicting distorted tracer concentrations. By  
99 contrast, when using a flux-form transport algorithm, the total tracer mass is conserved  
100 and thus the issue of mass losses can be eliminated, provided the flow is conservative.  
101 The use of numerical schemes with limiters leads to distorted tracer concentrations and  
102 affects the linearity. Thus, to accurately calculate the tracer concentration in a forward  
103 simulation and to use the model in inverse modeling, we employed a flux-form version  
104 of the global off-line, three-dimensional chemical NIES TM.

105 The synoptic and seasonal variability in XCO<sub>2</sub> is driven mainly by changes in surface  
106 pressure, the tropospheric volume-mixing ratio (VRM) and the stratospheric  
107 concentration, which is affected in turn by changes in tropopause height. The effects of  
108 variations in tropopause height are more pronounced with increasing contrast between  
109 stratospheric concentrations. Many CTMs demonstrate some common failings of model  
110 transport in the stratosphere (Hall et al. 1999). The difficulty of accurately representing

111 dynamical processes in the upper troposphere (UT) and lower stratosphere (LS) has  
112 been highlighted in recent studies (Mahowald et al., 2002; Wauch and Hall, 2002;  
113 Monge-Sanz et al., 2007). While there are many contributing factors, the principal  
114 factors affecting model performance in vertical transport are meteorological data and  
115 the vertical grid layout (Monge-Sanz et al., 2007).

116 The use of different meteorological fields in driving chemical transport models can  
117 lead to **diverse** distribution of chemical species in the UTLS region (Douglass et al.,  
118 1999). The quality of wind data provided by numerical weather predictions is another  
119 crucial factor for tracer transport (Jöckel et al., 2001; Stohl et al., 2004; Bregman et al.,  
120 2006). Wind fields produced by the Data Assimilation System (DAS) are commonly  
121 used for driving CTMs. Spurious variability, or “noise”, introduced via the assimilation  
122 procedure affects the quality of meteorological data through a lack of suitable  
123 observations, or by the inaccurate treatment of model biases (Bregman et al., 2006).  
124 This negative effect is proportional to the dynamic time scale and increases with  
125 operational time. The most sensitive area in this regard is the lower stratosphere in  
126 tropical regions, where large volumes of air move upward from the troposphere to the  
127 stratosphere. A lack of observations makes this region the most challenging in terms of  
128 data assimilation. **Bregman et al. (2006) pointed that additional difficulties for detecting**  
129 **model biases are caused by the fact that tropical atmosphere is not in geostrophic**  
130 **balance.** Schoeberl et al. (2003) suggested that GEOS DAS (Geodetic Earth Orbiting  
131 Satellite Data Assimilation System) is less suitable for long-term stratospheric transport  
132 studies than wind from a general circulation model. At the same time, improvements to

133 the data assimilation system itself (ECMWF ERA-Interim reanalysis; Dee and Uppala,  
134 2009) and the development of special products for use in transport models (MERRA:  
135 Modern Era Retrospective-analysis for Research and Applications; Bosilovich et al.,  
136 2008) have assisted in improving the accuracy of atmospheric circulation when using  
137 off-line models (Monge-Sanz et al., 2007).

138 Belikov et al. (2013) evaluated the simulated column-averaged dry air mole fraction  
139 of atmospheric carbon dioxide ( $X_{CO_2}$ ) against daily ground-based high-resolution  
140 Fourier Transform Spectrometer (FTS) observations measured at twelve sites of the  
141 Total Column Observing Network (TCCON), which provides an essential validation  
142 resource for the Orbiting Carbon Observatory (OCO), SCIAMACHY, and GOSAT. In  
143 this manuscript, **we present the application of the standard version of isentropic**  
144 **transport model** with HIAPER Pole-to-Pole Observations (HIPPO) Merged 10-second  
145 Meteorology, Atmospheric Chemistry, and Aerosol Data, which are highly time-  
146 resolved, because of the underlying 1-second in situ frequency measurement, and  
147 vertically-resolved, because of the GV flight plans that performed 787 vertical  
148 ascents/descents from the ocean/ice surface up to the tropopause. The remainder of this  
149 paper provides the model information and a detailed description of the meteorology  
150 dataset and HIPPO data, and a validation of the  $CO_2$  vertical profiles comparing against  
151 the HIPPO observations, followed by a discussion and conclusions.

## 152 **2 Model features and operation**

153 In this section, we describe the features and use of the NIES TM (denoted NIES-08, li).

154 As Belikov et al. (2011, 2013) described, the latest improved version of the NIES TM

155 model uses the ( $\theta$ - $\sigma$ ) hybrid sigma-isentropic vertical coordinate that is isentropic in  
156 the UTLS region but terrain-following in the free troposphere. This designed coordinate  
157 helps to simulate vertical motion in the isentropic part of the grid above level 350K.  
158 Basic physical model features include the flux-form dynamical core with a third-order  
159 van Leer advection scheme, a reduced latitude-longitude grid, a horizontal flux-  
160 correction method for mass balance, and turbulence parameterization.

## 161 **2.1 Meteorological data used in the simulation**

162 The NIES TM is an off-line model driven by Japanese reanalysis data, which covers  
163 more than 30 years from 1 January 1979 to present (Onogi et al., 2007). The period of  
164 1979-2004 is covered by the Japanese 25-year Reanalysis (JRA-25), used by Belikov  
165 et al. (2013), and is the product of the Japan Meteorological Agency (JMA) and Central  
166 Research Institute of Electric Power Industry (**CRIEPI**). After 2005, near real-time  
167 operational analysis, employing the same assimilation system as JRA-25, has been  
168 continued as the JMA Climate Data Assimilation System (JCDAS). The JRA-  
169 25/JCDAS dataset is distributed on a Gaussian horizontal grid T106 (320×160) with 40  
170 hybrid  $\sigma$ -p levels. The 6-hourly time step of JRA-25/JCDAS is coarser than the 3-  
171 hourly data from the National Centers for Environmental Prediction (NCEP) Global  
172 Forecast System (GFS) and Global Point Value (GPV) datasets, which were used in the  
173 previous model version (Belikov et al., 2011). However, with a better vertical resolution  
174 (40 levels on a hybrid  $\sigma$ -p grid versus 25 and 21 pressure levels for GFS and GPV,  
175 respectively) it is possible to implement a vertical grid with 32 levels (versus the 25  
176 levels used before), resulting in a more detailed resolution of the boundary layer and

177 UTLS region (Table 1).

178 The 2-D monthly distribution of the climatological heating rate, used to calculate  
179 vertical transport in the  $\theta$ -coordinate domain of the hybrid sigma-isentropic coordinate,  
180 is prepared from JCDAS reanalysis data, which are provided as the sum of short- and  
181 long-wave components on pressure levels.

182

## 183 **2.2 HIPER Pole-to-Pole data**

184 The HIPPO study investigated the carbon cycle and greenhouse gases at various  
185 **altitudes** (from 0 to 16 km) in the western hemisphere through the annual cycle. HIPPO  
186 is supported by the National Science Foundation (NSF) and its operations are managed  
187 by the Earth Observing Laboratory (EOL) of the National Center for Atmospheric  
188 Research (NCAR). Its base of operations is the EOL Research Aviation Facility (RAF)  
189 at the Rocky Mountain Metropolitan Airport (RMMA) in Jefferson County, Colorado.  
190 The main goal of HIPPO was to determine the global distribution of CO<sub>2</sub> and other  
191 trace atmospheric gases by sampling at several altitudes and latitudes (from 0 to 16 km,  
192 87.0N to -67.2S) in the Pacific Basin.

193 The dataset used in this paper includes the merged 10-second data product of  
194 meteorological, atmospheric chemistry, and aerosol measurements from three HIPPO  
195 Missions 1 to 3. The three missions took place from January, 2009 to April, 2010;  
196 HIPPO-1 (20090109–20090126), HIPPO-2 (20091102–20091122), and HIPPO-3  
197 (20100324–20100415), ranging from 128.0E to -84.0W, and 87.0N to -67.2S (Table 2).

198 All data are provided in a single space-delimited format ASCII file

199 ([https://www.eol.ucar.edu/field\\_projects/hippo](https://www.eol.ucar.edu/field_projects/hippo)).

200 HIPPO measured atmospheric constituents along transects running approximately  
201 pole-to-pole over the Pacific Ocean and recorded hundreds of vertical profiles from the  
202 ocean/ice surface up to the tropopause five times during four seasons from January,  
203 2009 to September, 2011. HIPPO provides the first high-resolution vertically resolved  
204 global survey of a comprehensive suite of atmospheric trace gases and aerosols  
205 pertinent to understanding the carbon cycle and challenging global climate models. The  
206 10-second merge product applied in this study was derived by combining the National  
207 Science foundation (NSF)/NCAR GV aircraft navigation and atmospheric structure  
208 parameters including position, time, temperature, pressure, and wind speed reported at  
209 1-second frequency, with meteorological, atmospheric chemistry and aerosol  
210 measurements made by several teams of investigators on a common time and position  
211 basis.

### 212 **2.3 Model setup**

213 The standard model was run with the three HIPPO missions to study atmospheric tracer  
214 transport and the ability of the model to reproduce the column-averaged dry air mole  
215 fractions and vertical profile of atmospheric CO<sub>2</sub>. **The model was run at a horizontal  
216 resolution of 2.5 °×2.5 ° and 32 vertical levels from the surface to 3 hPa.**

217 The CO<sub>2</sub> simulations were began on January 1, 2009, November 1, 2009 and March  
218 1, 2010 for the three HIPPO missions 1 to 3, respectively, with individual initial 3D  
219 tracer distributions using the **global prior fluxes of biosphere-atmosphere and air-ocean  
220 exchange, fossil fuel emissions, biomass burning, and GOSAT Level 4A inverse model**

221 correction (Maksyutov et al., 2013), provided by climatological mean of monthly global  
222 CO<sub>2</sub> fluxes estimated with GLOBALVIEW and GOSAT SWIR Level 2 XCO<sub>2</sub> data. As  
223 we use same set of fluxes and same version of transport model as GOSAT Level 4  
224 product, the flux corrections provided by GOSAT Level 4 product provide optimal fit  
225 to available observations.

### 226 **3 Discussions**

227 The current model versions have been used in several tracer transport studies and  
228 were evaluated through participation in transport model intercomparisons (Niwa et al.,  
229 2011; Patra et al., 2011). The simulation results of the tracer transport model show  
230 consistency with observations in the near-surface layer and in the free troposphere.  
231 However, the model performance in the UTLS region has not been evaluated in detail  
232 against other observations.

#### 233 **3.1 Comparison with CO<sub>2</sub> observations**

234 Figure 1 show the scatters diagram of modeled results versus total column of HIPPO-  
235 1, 2, 3. The majority of points are within a 95% confidence interval of total CO<sub>2</sub> column  
236 concentration. Modeled HIPPO-1's precision successively exceeds 2 and 3, inferring  
237 the simulation results with the relevant either seasonal changes or data quality.

238 The simulation results of CO<sub>2</sub> concentration time-varying for HIPPO-1 using the  
239 standard model display good performance and weak dispersion of concentrations. The  
240 validation results (Figure 2(a)) show that approximately 69.2% of the absolute biases  
241 are within 1 ppmv, approximately 92.3% are within 2 ppmv, and only 7.7% exceed 3  
242 ppmv. Furthermore, as shown by the root-mean-square error (RMSE) with time, during

243 most days in January the model values' dispersion was small compared with the  
244 observed values, apart from the first few days of the month. According to the simulation  
245 results of the HIPPO-1 observed and simulated latitude-varying CO<sub>2</sub> concentration data,  
246 the comparison values always underestimate the atmospheric XCO<sub>2</sub>, and the  
247 differences are all within 1.5 ppmv in the Southern Hemisphere, and vice versa in the  
248 Northern Hemisphere with 85.8% of the differences under 1.1 ppmv. Figure 2(b) shows  
249 that the larger biases usually occur in the Northern Hemisphere high latitudes. The  
250 RMSE also reflects the instability of the simulated values in the Northern Hemisphere  
251 high latitudes.

252 For HIPPO-2 data from November 2 to 22, 2009, the absolute biases of observed and  
253 simulated time-varying are all within 2 ppmv, and 77.8 % of the differences are less  
254 than 1 ppmv (Figure 2(c)). Approximately 5/6 of the data over the month show  
255 comparative stability. Similarly with HIPPO-1, the simulation results are always  
256 underestimates in the Southern Hemisphere and overestimates in the Northern  
257 Hemisphere. As shown in Figure 2(d), the complete simulation displays good  
258 performance, apart from one day in the Northern Hemisphere high latitudes. In the same  
259 manner, the RMSE shows good stability in the Southern Hemisphere, in particular for  
260 the low-to mid-latitudes of the Southern Hemisphere. The model also simulates well in  
261 the Northern Hemisphere, especially from 45 ° to 70 °N.

262 Based on HIPPO-3 data from March 24 to April 15, 2010, the model simulation  
263 overestimates in March and underestimates in April. As shown in Figure 2(e), in March,  
264 the biases over several days were over 2 ppmv, and one of these days exceeded 3 ppmv.

265 However, the absolute biases were all within 2 ppmv in April, and 75% of the absolute  
266 biases were less than 1 ppmv, which suggests relatively good performance by the model  
267 simulation. As shown by the RMSE, the data for the last days in March were **disperse**.  
268 However, 81.8% of the data in April showed comparatively good stability. The absolute  
269 biases are all under 1.5 ppmv in the Southern Hemisphere, and are also within 2 ppmv  
270 for the low- and mid-latitudes of the Northern Hemisphere (Figure 2(f)).However, a  
271 relatively large difference occurs at the Northern Hemisphere high latitudes, at one  
272 point exceeding 3 ppmv. Furthermore, the RMSE become greater with latitude from  
273 the Southern to Northern hemisphere, inferring the simulation results are increasingly  
274 **disperse** with increasing latitude.

### 275 **3.2 Validation of CO<sub>2</sub> vertical profiles**

276 The GV flight plan performed 787 vertical ascents/descents from the ocean/ice  
277 surface/land surface to the tropopause. Two maximum altitude ascents were planned  
278 per flight to the tropopause/LS; one in the first half and the other in the second half of  
279 the research flight. In between, several vertical profiles from below the PBL to the mid-  
280 troposphere (1000–28000 feet) were flown. Profiles were flown approximately every  
281 2.2 °of latitude with 4.4 °between consecutive near-surface or high-altitude samples.  
282 Rate of climb and descent was 1500 ft/minute (457m/minute). During these profiles,  
283 the GV averaged a ground speed of approximately 175m/second, or 10 km/minute.

284 Most of a flight was conducted below the international Reduced Vertical Separation  
285 Minimum (RVSM), usually 29000 ft or 8850 m, to allow the GV to descend and climb  
286 constantly to collect data at different altitudes throughout the troposphere. All flight

287 plans were subject to modifications depending on local atmospheric conditions and  
288 approval by air traffic control. Most profiles extended from approximately 300 to 8500  
289 m altitude, constrained by air traffic, but significant profiling extended above  
290 approximately 14 km.

291 One of the aims of this paper was to validate the model column-averaged  
292 concentration against the typical HIPPO flight plans, and we therefore examined the  
293 variability of CO<sub>2</sub> concentrations with HIPPO merged 10-second meteorology,  
294 atmospheric chemistry, and aerosol measurements from Mission 1 to 3. For each  
295 mission, several hundred vertical profiles were produced. We have only selected the  
296 vertical profiles from near-surface to LS to compare the simulations using the standard  
297 model with observations. Each mission can be divided into six parts for analysis; the  
298 low-, mid- and high-latitudes in the Southern and Northern hemispheres, respectively.

299 The above Figure 3 presents us the change of flight altitude and bias by subtracting  
300 observation by simulation of HIPPO-1, 2, 3 with latitude. The observations' number of  
301 these three missions is 17621, 23451, 22372 respectively, and the plenty of observations  
302 provide basis for model validation. Based on the change of flight height with latitude  
303 in the Figure 3, we only select CO<sub>2</sub> profiles that their height is from near surface to  
304 lower stratosphere. According to the above rule, 24, 34, 35 profiles are chosen  
305 respectively for the HIPPO-1, 2, 3. Then we separately choose one profile in the low,  
306 middle and high latitude of Northern and Southern hemisphere from the selected  
307 profiles for each mission because of the similarity of the profile shape in every latitude  
308 zone. Seen from the Figure 3, the relatively larger biases repeatedly occur in the higher  
309 latitude of Northern hemisphere.

310 For HIPPO-1, the modeled value is always less than the observation value in  
311 the Southern Hemisphere and vice versa in the Northern Hemisphere. The bias is less  
312 than 2 ppmv for the entire profile from the near-surface to the LS; however, it increases  
313 from 2 to 4 ppmv above 10 km covering the Northern Hemisphere high latitudes.

314 Figure 4 shows the comparison of simulation results and observations for data from  
315 the near-surface to the LS in the low-, mid- and high- latitude. In the low-latitudes, as  
316 shown by panel 4(c) and (d), the simulation performed very well compared with  
317 observations. With the exception of the biases of approximately 2 ppmv in the  
318 tropopause in panel 4(d), the biases are all within 1 ppmv. In the mid- and high- latitudes,  
319 it is different in both hemispheres. In the Southern Hemisphere, the majority biases are  
320 within 2 ppmv apart from the LS zone in Figure 4(a) and 2 to 6 km region in panel 4(b).  
321 In the Northern Hemisphere (panel 4(e) and (f)), the simulated vertical profiles show  
322 good performances, apart from UTLS, and the biases are less than 2 ppmv. Some large  
323 biases occurred in the UTLS exceeding 4 ppmv when the potential temperature gradient  
324 increased rapidly with height. For details, Figure 5 presents us the biases of simulation  
325 minus observation corresponding to Figure 4(a) – 4(f) respectively.

326 HIPPO-2 data showed overall similarity with HIPPO-1 data based on the distribution  
327 of positive and negative bias. However, an anomaly occurred at approximately -60 °and  
328 75 ° latitude, showing positive and negative biases, respectively, some exceeding 6  
329 ppmv. Figure 6(a) is the vertical profile of the Southern Hemisphere high latitudes,  
330 which clearly shows that the simulation matches well with the observations from the  
331 near-surface to the tropopause. However, large biases occur above 8 km; panel 6(b) also

332 shows this phenomenon above 10 km. In the low latitudes (Figure 6(c) and (d)), the  
333 simulations match well with observations. The potential temperature gradient is smooth  
334 and the biases are less than 1 ppmv from near-surface to the UT, which indicates good  
335 performance. For the mid-latitudes of the Northern Hemisphere, panel 6(e) shows  
336 relatively good simulation performance. However, as shown in panel 6(f), the high  
337 latitudes did not perform well in the near-surface or the low- and mid-troposphere.  
338 Compared with observations, the simulation profiles do not appear to reflect the original  
339 shape. Moreover, Figure 7 further displays the biases of simulation minus observation  
340 corresponding to Figure 6(a) – 6(f) respectively.

341 As shown by HIPPO-3 data the biases increase abruptly with flight height for the  
342 mid- to high-latitudes of the Northern Hemisphere with values reaching 7 ppmv. In the  
343 high-latitudes of the Southern Hemisphere (panel 8(a)) the simulation underestimates  
344 the observations, and the absolute biases are isostatic from the near-surface to the LS,  
345 which are less than 3 ppmv. The Southern Hemisphere low latitudes (panel 8(c))  
346 indicate good performance of the simulations, where all the biases are less than 1 ppmv.  
347 In the Northern Hemisphere low latitudes (panel 8(d)), the entire simulation appears to  
348 match well with observations. However, some locations do not reproduce the precise  
349 shape through the entire height. For the mid- to high- northern latitudes (panel 8(e) and  
350 (f)), the simulations performed relatively well from the near-surface to the UT.  
351 Furthermore, Figure 9 shows the biases of simulation minus observation corresponding  
352 to Figure 8(a) – 8(f) respectively.

353 Larger bias in simulations is found in the winter lower stratosphere in the northern  
354 high-latitudes. The problem appears because between tropopause and 350 K level  
355 model uses vertical wind provided by reanalysis instead of using radiative heating rate,  
356 which is more accurate in stratosphere (Weaver et al, 1993, Belikov et al., 2013).  
357 Extending the isentropic coordinates to mid-troposphere levels such as implemented by  
358 Chen and Rasch, (2011), Bleck et al (2015) has potential for reducing the transport bias  
359 in this region and season. The positive bias can reach level of 4 ppm for CO<sub>2</sub>. However,  
360 this problem only affects simulations for observation made in lower stratosphere in high  
361 latitudes in cold season when the tropopause level is low. However the number of in-  
362 situ observations made in this altitude is very limited. The satellite observations of the  
363 total column such as GOSAT are also reduced considerably in high latitudes in cold  
364 season (Yoshida et al, 2013). Thus this lower stratosphere bias is not likely to deteriorate  
365 the transport model performance in the inverse modeling applications (Maksyutov et  
366 al., 2013). However, these biased values probably result in greater errors of a flux  
367 inversion with signals being transported into lower latitudes in adverse synoptic  
368 patterns.

#### 369 **4 Conclusions**

370 This study tested and verified the ability of a chemistry transport model to reproduce  
371 CO<sub>2</sub> vertical profiles using HIPPO merged 10-second meteorology, atmospheric  
372 chemistry, and aerosol data from Missions 1 to 3, which span three different seasons  
373 (autumn, winter and spring). The results show that the model somewhat underestimates  
374 CO<sub>2</sub> in the Southern Hemisphere and overestimates it in the Northern Hemisphere for

375 these three missions. However, the model was able to reproduce the seasonal and inter-  
376 annual variability of CO<sub>2</sub> with RMS bias across all profiles with a level of 0.9 ppmv.  
377 The model performed well from the near-surface layer to the top of the troposphere,  
378 apart from the lower stratosphere the high latitude regions, in particular, in the Northern  
379 Hemisphere in spring, where large biases would often appear. **The smaller bias for**  
380 **HIPPO-1 compared with HIPPO-3 arises from seasonal changes in synoptic patterns**  
381 **from January to March and April, as simulated by Patra et al. (2008).**

382 The accuracy of these calculations will increase with the adaptation of the mass-  
383 balanced reanalysis data (MERRA, Bosilovich et al., 2008). **This off-line model with**  
384 **horizontal flux-correction attain mass conservation because vertically integrated mass**  
385 **change is in balance with the surface pressure tendency (Belikov et al., 2011). The**  
386 **computation achieve fast convergence with CO<sub>2</sub> distribution tending towards stability**  
387 **in the whole integral height.** Demand for global high-resolution fields of CO<sub>2</sub> and other  
388 greenhouse gases will also increase because of their use as a priori information in  
389 retrieval algorithms of observation instruments, such as the AIRS satellite (e.g., Strow  
390 and Hannon, 2008) and GOSAT (e.g., Yokota et al., 2009), and regional inverse  
391 modeling studies (Thompson, et al., 2014). **Employing HIPPO-1, 2, 3, validation of the**  
392 **NIES model provide basis for applying high-precision satellite product, and so we can**  
393 **get more and better carbon sources/sinks information.**

394 **Acknowledgements** The authors acknowledge **NSF, EOL of NCAR and NOAA which**  
395 **supported the collection of the original HIPPO data.** This project was supported by the  
396 National Basic Research Program of China (No. 2010CB951603). The computation

397 was supported by the High Performance Computer Center of East China Normal  
398 University. We thank the team members of the Biogeochemical Cycle Modeling and  
399 Analysis Section of National Institute for Environment Studies, Tsukuba, Japan for  
400 providing expert advice and assistance. The GOSAT Level 4 data made available by  
401 GOSAT project ([http://www.gosat.nies.go.jp/index\\_e.html](http://www.gosat.nies.go.jp/index_e.html)).

402

403

404

405

406

407

408

409

410

411

412

413

414

415

416

417

418

419 **References**

- 420 1. Baker, D. F., Law, R. M., Gurney, K. R., Rayner, P., Peylin, P., Denning, A. S.,  
421 Bousquet, P., Bruhwiler, L., Chen, Y.-H., Ciais, P., Fung, I. Y., Heimann, M., John,  
422 J., Maki, T., Maksyutov, S., Masarie, K., Prather, M., Pak, B., Taguchi, S., and Zhu,  
423 Z.: TransCom 3 inversion intercomparison: Impact of transport model errors on the  
424 interannual variability of regional CO<sub>2</sub> fluxes 1988–2003, *Global Biogeochem. Cy.*,  
425 20, GB1002, doi:10.1029/2004GB002439, 2006.
- 426 2. Belikov, D. A., Maksyutov, S., Miyasaka, T., Saeki, T., Zhuravlev, R., and  
427 Kiryushov, B., Mass-conserving tracer transport modeling on a reduced latitude-  
428 longitude grid with NIES-TM, *Geosci. Model Dev.*, 4, 207-222, doi: 10.5194/gmd-  
429 4-207-2011, 2011.
- 430 3. Belikov, D. A., Maksyutov, S., Sherlock, V., Aoki, S., Deutscher, N. M., Dobe, S.,  
431 Griffith, D., Kyro, E., Morino, I., Nakazawa, T., Notholt, J., Rettinger, M.,  
432 Schneider, M., Sussmann, R., Toon, G. C., Wennberg, P. O., and Wunch, D.,  
433 Simulations of column-averaged CO<sub>2</sub> and CH<sub>4</sub> using the NIES TM with a hybrid  
434 sigma-isentropic ( $\sigma - \theta$ ) vertical coordinate, *Atmos. Chem. Phys.*, 13, 1713-1732,  
435 doi: 10.519/acp-13-1713-2013, 2013.
- 436 4. Bleck, R., Bao, J.-W., G. Benjamin, S., Brown, J. M., Fiorino, M., Henderson,  
437 T. B., Lee, J.-L., MacDonald, A. E., Madden, P., Middlecoff, J., Rosinski, J.,  
438 Smirnova, T. G., Sun, S., and N. Wang, A Vertically Flow-Following Icosahedral  
439 Grid Model for Medium-Range and Seasonal Prediction. Part I: Model Description.  
440 *Mon. Wea. Rev.*, 143, 2386–2403. doi: [20](http://dx.doi.org/10.1175/MWR-D-14-</a></p></div><div data-bbox=)

- 441        **00300.1, 2015**
- 442    5. Bolin, B., and Keeling, C. D., Large scale atmospheric mixing as deduced from  
443        seasonal and meridional variations of the atmospheric carbon dioxide, *J. Geophys.*  
444        *Res.*, vol.68, pp.3899-3920, 1963.
- 445    6. Bosilovich, M. G., Chen, J., Robertson F. R., and Adler R. F.: Evaluation of global  
446        precipitation in reanalysis. *J. Appl. Meteor. Climatol.*, 47, 2279–2299,  
447        doi:10.1175/2008JAMC1921.1, 2008.
- 448    7. Bregman, B., Meijer, E., and Scheele, R.: Key aspects of stratospheric tracer  
449        modeling using assimilated winds, *Atmos. Chem. Phys.*, 6, 4529–4543, doi:  
450        10.5194/acp-6-4529-2006, 2006.
- 451    8. **Chen, C.-C. and Rasch, P. J., Climate Simulations with an Isentropic Finite-Volume**  
452        **Dynamical Core. *J. Climate*, 25, 2843–2861. doi:**  
453        **<http://dx.doi.org/10.1175/2011JCLI4184.1>, 2012.**
- 454    9. Dee, D. P. and Uppala, S., Variational bias correction of satelliteradiance data in the  
455        ERA-Interim reanalysis, *Q. J. Roy. Meteorol. Soc.*, 135, 1830–1841, 2009.
- 456    10. Denning, A. S., Randall, D. A., Collatz, G. J., and Sellers, P. J.: Simulations of  
457        terrestrial carbon metabolism and atmospheric CO<sub>2</sub> in a general circulation model.  
458        II. Simulated CO<sub>2</sub> concentrations, *Tellus B Chem. Phys. Meteorol.*, 48, 543–567,  
459        doi:10.1034/j.1600-0889.1996.t01-1-00010.x, 1996.
- 460    11. Denning, A. S., Holzer, M., Gurney, K. R., Heimann, M., Law, R. M., Rayner, P.  
461        J., Fung, I. Y., Fan, S.-M., Taguchi, S., Friedlingstein, P., Balkanski, Y., Taylor, J.,  
462        Maiss, M., and Levin, I.: Three-dimensional transport and concentration of SF<sub>6</sub>: A

- 463 model intercomparison study (TransCom2), *Tellus*, 51B, 266–297, 1999.
- 464 12. Douglass, A. R., Prather, M. J., Hall, T. M., Strahan, S. E., Rasch, P. J., Sparling,  
465 L. C., Coy, L., and Rodriguez J. M.: Choosing meteorological input for the global  
466 modeling initiative assessment of high-speed aircraft, *J. Geophys. Res.*, 104,  
467 27545–27564, 1999.
- 468 13. GLOBALVIEW-CO<sub>2</sub>: Cooperative Atmospheric Data Integration Project–Carbon  
469 Dioxide, CD-ROM, NOAA ESRL, Boulder, Colorado, 2010.
- 470 14. Gurney, K. R., Law, R. M., Denning, A. S., Rayner, P. J., Pak, B. C., Baker, D.,  
471 Bousquet, P., Bruhwiler, L., Chen, Y. H., Ciais, P., Fung, I. Y., Heimann, M., John,  
472 J., Maki, T., Maksyutov, S., Peylin, P., Prather, M., and Taguchi, S.: Transcom 3  
473 inversion intercomparison: Model mean results for the estimation of seasonal  
474 carbon sources and sinks, *Global Biogeochem. Cy.*, 18, GB1010,  
475 doi:10.1029/2003GB002111, 2004.
- 476 15. Hack, J. J., Boville, B. A., Briegleb, B. P., Kiehl, J. T., Rasch, P. J., and Williamson,  
477 D. L.: Description of the NCAR community climate model (CCM2), NCAR/TN-  
478 382, 108, Climate and Global Dynamics Division, NCAR, Boulder, Colorado,  
479 USA, 1993.
- 480 16. Hall, T. M., Waugh, D.W., Boering, K. A., and Plumb R. A.: Evaluation of transport  
481 in stratospheric models, *J. Geophys. Res.*, 104, 18815–18839, 1999.
- 482 17. Hein, R., Crutzen, P. J., and Heimann, M., An inverse modeling approach to  
483 investigate the global atmospheric methane cycle, *Global Biogeochem Cycles*, vol,  
484 11, pp.43-76, 1997.

- 485 18. Ciais, P., Sabine C., Bala G., Bopp L., Brovkin V., Canadell J., Chhabra A., DeFries  
486 R., Galloway J., Heimann M., Jones C., Le Quéré C., Myneni R. B., Piao S. and  
487 Thornton P., 2013: Carbon and Other Biogeochemical Cycles. In: Climate Change  
488 2013: The Physical Science Basis. Contribution of Working Group I to the Fifth  
489 Assessment Report of the Intergovernmental Panel on Climate Change [Stocker,  
490 T.F., D. Qin, G.-K. Plattner, M. Tignor, S.K. Allen, J. Boschung, A. Nauels, Y. Xia,  
491 V. Bex and P.M. Midgley (eds.)]. Cambridge University Press, Cambridge, United  
492 Kingdom and New York, NY, USA.
- 493 19. Jacob, D., Prather, M. J., Rasch, P. J., Shea, R.-L., Balkanski, Y. J., Beagley, S. R.,  
494 Bergmann, D. J., Blackshear, W. T., Brown, M., Chiba, M., Chipperfield, M. P., de  
495 Grandpré, J., Dignon, J. E., Feichter, J., Genthon, C., Grose, W. L., Kasibhatla, P.  
496 S., Köhler, I., Kritz, M. A., Law, K., Penner, J. E., Ramonet, M., Reeves, C. E.,  
497 Rotman, D. A., Stockwell, D. Z., Van Velthoven, P. F. J., Verver, G., Wild, O., Yang,  
498 H., and Zimmermann, P.: Evaluation and intercomparison of global transport  
499 models using <sup>222</sup>Rn and other short-lived tracers, *J. Geophys. Res.*, 102(D5),  
500 5953–5970, 1997.
- 501 20. Jöckel, P., von Kuhlmann, R., Lawrence, M. G., Steil, B., Brenninkmeijer, C. A.  
502 M., Crutzen, P. J., Rasch, P. J., and Eaton, B.: On a fundamental problem in  
503 implementing flux-form advection schemes for tracer transport in 3-dimensional  
504 general circulation and chemistry transport models, *Q. J. Roy. Meteorol. Soc.*, 127,  
505 1035–1052, 2001.
- 506 21. Keppel-Aleks, G., Wennberg, P. O., and Schneider, T.: Sources of variations in total

507 column carbon dioxide, *Atmos. Chem. Phys.*, 11, 3581–3593, doi: 10.5194/acp-11-  
508 3581-2011, 2011.

509 22. Law, R. M., Peters, W., Rödenbeck, C., Aulagnier, C., Baker, I., Bergmann, D. J.,  
510 Bousquet, P., Brandt, J., Bruhwiler, L., Cameron-Smith, P. J., Christensen, J. H.,  
511 Delage, F., Denning, A. S., Fan, S.-M., Geels, C., Houweling, S., Imasu, R.,  
512 Karstens, U., Kawa, S. R., Kleist, J., Krol, M., Lin, S.-J., Lokupitiya, R., Maki, T.,  
513 Maksyutov, S., Niwa, Y., Onishi, R., Parazoo, N., Patra, P. K., Pieterse, G., Rivier,  
514 L., Satoh, M., Serrar, S., Taguchi, S., Takigawa, M., Vautard, R., Vermeulen, A. T.,  
515 and Zhu, Z.: Trans Commodel simulations of hourly atmospheric CO<sub>2</sub>:  
516 Experimental overview and diurnal cycle results for 2002, *Global Biogeochem. Cy.*,  
517 22, GB3009, doi:10.1029/2007GB003050, 2008.

518 23. Mahowald, N. M., Plumb, R. A., Rasch, P. J., del Corral, J., and Sassi, F.:  
519 Stratospheric transport in a three-dimensional isentropic coordinate model, *J.*  
520 *Geophys. Res.*, 107, 4254, doi:10.1029/2001JD001313, 2002.

521 24. Maksyutov, S., Patra, P. K., Onishi, R., Saeki, T., and Nakazawa, T., NIES/FRCGC  
522 global atmospheric tracer transport model: description, validation, and surface  
523 sources and sinks inversion, *Journal of the Earth Simulator*, 9, 3-18, 2008.

524 25. Maksyutov, S., Takagi, H., Valsala, V. K., Saito, M., Oda, T., Saeki, T., Belikov, D.  
525 A., Saito, R., Ito, A., Yoshida, Y., Morino, L., Uchino, O., Andres, R. J., and Yokota,  
526 T., Regional CO<sub>2</sub> flux estimates for 2009-2010 based on GOSAT and ground-based  
527 CO<sub>2</sub> observations, *Atmos. Chem. Phys.*, 13, 93519373, doi: 10.5194/acp-13-9351-  
528 2013, 2013.

- 529 26. Monge-Sanz, B. M., Chipperfield, M. P., Simmons, A. J., and Uppala, S. M., Mean  
530 age of air and transport in a CTM: Comparison of different ECMWF analyses,  
531 *Geophys. Res. Lett.*, 34, L04801, doi: 10.1029/2006GL028515, 2007.
- 532 27. Niwa, Y., Patra, P. K., Sawa, Y., Machida, T., Matsueda, H., Belikov, D., Maki, T.,  
533 Ikegami, M., Imasu, R., Maksyutov, S., Oda, T., Satoh, M., and Takigawa, M.:  
534 Three-dimensional variations of atmospheric CO<sub>2</sub>: aircraft measurements and  
535 multi transport model simulations, *Atmos. Chem. Phys.*, 11, 13359–13375,  
536 doi:10.5194/acp-11-13359-2011, 2011.
- 537 28. Onogi, K., Tsutsui, J., Koide, H., Sakamoto, M., Kobayashi, S., Hatsushika, H.,  
538 Matsumoto, T., Yamazaki, N., Kamahori, H., Takahashi, K., Kadokura, S., Wada,  
539 K., Kato, K., Oyama, R., Ose, T., Mannoji, N., and Taira, R.: The JRA-25  
540 Reanalysis, *J. Met. Soc. Jap.*, 85, 369–432, 2007.
- 541 29. Parker, R., Boesch, H., Cogan, A., Fraser, A., Feng, L., Palmer, P.I., Messerschmidt,  
542 J., Deutscher, N., Griffith, D. W. T., Notholt, J., Wennberg, P.O., and Wunch, D.:  
543 Methane observations from the Greenhouse Gases Observing SATellite:  
544 Comparison to ground based TCCON data and model calculations, *Geophys. Res.*  
545 *Lett.*, 38, L15807, doi: 10.1029/2011GL047871, 2011.
- 546 30. Patra, P. K., Baker, D., Bousquet, P., Bruhwiler, L., Chen, Y.-H., Ciais, P., Denning,  
547 S. A., Fan, S., Fung, I. Y., Gloor, M., Gurney, K., Heimann, M., Higuchi, K., John,  
548 J., Maki, T., Maksyutov, S., Peylin, P., Prather, M., Pak, B., Sarmiento, J., Taguchi,  
549 S., Takahashi, T., and Yuen, C.-W.: Sensitivity of optimal extension of observation  
550 networks to the model transport, *Tellus*, 55B, 498–511, 2003a.

- 551 31. Patra, P. K., Maksyutov, S., Sasano, Y., Nakajima, H., Inoue, G., and Nakazawa, T.:  
552 An evaluation of CO<sub>2</sub> observations with Solar Occultation FTS for Inclined-Orbit  
553 Satellite sensor for surface source inversion, *J. Geophys. Res.*, 108(D24), 4759,  
554 doi:10.1029/2003JD003661, 2003b.
- 555 32. Patra, P. K., Peters, W., R ödenbeck, C., Aulagnier, C., Baker, I., Bergmann, D. J.,  
556 Bousquet, P., Brandt, J., Bruhwiler, L., Cameron-Smith, P. J., Christensen, J. H.,  
557 Delage, F., Denning, A. S., Fan, S.-M., Geels, C., Houweling, S., Imasu, R.,  
558 Karstens,U., Kawa, S. R., Kleist, J., Krol, M., Law, R. M., Lin, S.- J., Lokupitiya,  
559 R., Maki, T., Maksyutov, S., Niwa, Y., Onishi, R., Parazoo, N., Pieterse, G., Rivier,  
560 L., Satoh, M., Serrar, S., Taguchi, S., Takigawa, M., Vautard, R., Vermeulen, A. T.,  
561 and Zhu, Z., TransCom model simulations of hourly atmospheric CO<sub>2</sub>: Analysis of  
562 synoptic-scale variations for the period 2002–2003, *Global Biogeochem. Cy.*, 22,  
563 GB4013, doi:10.1029/2007GB003081, 2008.
- 564 33. Patra, P. K., Houweling, S., Krol, M., Bousquet, P., Belikov, D., Bergmann, D.,  
565 Bian, H., Cameron-Smith, P., Chipperfield, M. P., Corbin, K., Fortems-Cheiney, A.,  
566 Fraser, A., Gloor, E., Hess, P., Ito, A., Kawa, S. R., Law, R. M., Loh, Z., Maksyutov,  
567 S., Meng, L., Palmer, P. I., Prinn, R. G., Rigby, M., Saito, R., and Wilson, C.:  
568 Transcom model simulations of CH<sub>4</sub> and related species: linking transport, surface  
569 flux and chemical loss with CH<sub>4</sub> variability in the troposphere and lower  
570 stratosphere, *Atmos. Chem. Phys.*, 11-12813-12837, doi: 10.5194/acp-11-12813-  
571 2011, 2011.
- 572 34. Rasch, P. J., Boville, B. A., and Brasseur, G. P.: A three dimensional general

- 573 circulation model with coupled chemistry for the middle atmosphere, *J. Geophys.*  
574 *Res.*, 100, 9041–9071, 1995.
- 575 35. Raupach, M. R., G. Marland, P. Ciais, C. Le Quere, J. G. Canadell, G. Klepper, and  
576 C. B. Field, Global and regional drivers of accelerating CO<sub>2</sub> emissions, *Proc. Natl.*  
577 *Acad. Sci. U.S.A.*, 104(24), 288–293, doi:10.1073/pnas.0700609104, 2007.
- 578 36. Rayner, P. J., Enting, I. G., Francey, R. J., and Langenfelds R., Reconstructing the  
579 recent carbon cycle from atmospheric CO<sub>2</sub>,  $\delta^{13}\text{C}$  and O<sub>2</sub>/N<sub>2</sub> observations, *Tellus*,  
580 vol. 51B, pp.213-232, 1999.
- 581 37. Rayner, P. J. and O'Brien, D. M.: The utility of remotely sensed CO<sub>2</sub> concentration  
582 data in surface inversion, *Geophys. Res. Lett.*, 28, 175–178, 2001.
- 583 38. Schoeberl, M. R., Douglass, A. R., Zhu, Z., and Pawson, S.: A comparison of the  
584 lower stratospheric age spectra derived from a general circulation model and two  
585 data assimilation systems, *J. Geophys. Res.*, 108, 4113, doi:  
586 10.1029/2002JD002652, 2003.
- 587 39. Scholes, R. J., Monteiro, P. M. S., Sabine, C. L., and Canadell, J. G.: Systematic  
588 long-term observations of the global carbon cycle, *Trends in Ecology & Evolution*,  
589 24, 427–430, doi:10.1016/j.tree.2009.03.006, 2009.
- 590 40. Stohl, A., Cooper, O., and James, P.: A cautionary note on the use of meteorological  
591 analysis data for quantifying atmospheric mixing, *J. Atmos. Sci.*, 61, 1446–1453,  
592 2004.
- 593 41. Strow, L. L. and Hannon, S. E.: A 4-year zonal climatology of lower tropospheric  
594 CO<sub>2</sub> derived from ocean-only Atmospheric Infrared Sounder observations, *J.*

- 595 Geophys. Res., 113, D18302, doi: 10.1029/2007JD009713, 2008.
- 596 42. Tans, P., Fung, I., and Takahashi, T., Observational constraints of the global  
597 atmospheric CO<sub>2</sub> budget, *Science*, vol. 247, pp.1431-1438, 1990.
- 598 43. Thompson, R. L., Ishijima, K., Saikawa, E., Corazza, M., Karstens, U., Patra, P. K.,  
599 Bergamaschi, P., Chevallier, F., Dlugokencky, E., Prinn, R. G., Weiss, R. F.,  
600 O'Doherty, S., Fraser, P. J., Steele, L. P., Krummel, P. B., Vermeulen, A., Tohjima,  
601 Y., Jordan, A., Haszpra, L., Steinbacher, M., Van der Laan, S., Aalto, T., Meinhardt,  
602 F., Popa, M. E., Moncrieff, J., and Bousquet, P., TransCom N<sub>2</sub>O model inter-  
603 comparison – Part 2: Atmospheric inversion estimates of N<sub>2</sub>O emissions, *Atmos.*  
604 *Chem. Phys.*, 14, 6177–6194, doi:10.5194/acp-14-6177-2014, 2014
- 605 44. Waugh, D. W., and Hall, T. M.: Age of stratospheric air: Theory, observations, and  
606 models, *Rev. Geophys.*, 40, 1010, doi: 10.1029/2000RG000101, 2002.
- 607 45. Weaver, C. J., Douglass, A. R., and Rood, R. B., Thermodynamic balance of three-  
608 dimensional stratospheric winds derived from a data assimilation procedure, *J.*  
609 *Atmos. Sc.*, 50, 2987-2993, 1993.
- 610 46. Wofsy, S. C., Daube, B. C., Jimenez, R., Kort, E., Pittman, J. V., Park, S., Commane,  
611 R., Xiang, B., Santoni, G., Jacob, D., Fisher, J., Pickett-Heaps, C., Wang, H., Wecht,  
612 K., Wang, Q.-Q., Stephens, B. B., Shertz, S., Watt, A. S., Romashkin, P., Campos,  
613 T., Haggerty, J., Cooper, W. A., Rogers, D., Beaton, S., Hendershot, R., Elkins, J.  
614 W., Fahey, D. W., Gao, R. S., Moore, F., Montzka, S. A., Schwarz, J. P., Perring, A.  
615 E., Hurst, D., Miller, B. R., Sweeney, C., Oltmans, S., Nance, D., Hints, E., Dutton,  
616 G., Watts, L. A., Spackman, J. R., Rosenlof, K. H., Ray, E. A., Hall, B., Zondlo, M.

617 A., Diao, M., Keeling, R., Bent, J., Atlas, E. L., Lueb, R., Mahoney M. J., 2012.  
618 HIPPO Merged 10-second Meteorology, Atmospheric Chemistry, Aerosol Data  
619 (R\_20121129). Carbon Dioxide Information Analysis Center, Oak Ridge National  
620 Laboratory, Oak Ridge, Tennessee, U.S.A.  
621 [http://dx.doi.org/10.3334/CDIAC/hippo\\_010](http://dx.doi.org/10.3334/CDIAC/hippo_010), (Release 20121129)  
622 (HIPPO\_all\_missions\_merge\_10s\_20121129.tbl).

623 47. Wunch, D., Toon, G., Blavier, J.-F. L., Washenfelder, R.A., Notholt, J., Connor,  
624 B.J., Griffith, D.W.T., Sherlock, V., and Wennberg, P.O.: The Total Carbon Column  
625 Observing Network (TCCON), *Phil. Trans. R. Soc. A* 369, 2087–2112,  
626 doi:10.1098/rsta.2010.0240, 2011.

627 48. Yang, Z., Washenfelder, R. A., Keppel-Aleks, G., Krakauer, N. Y., Randerson, J.  
628 T., Tans, P. P., Sweeney, C., and Wennberg, P. O.: New constraints on Northern  
629 Hemisphere growing season net flux P, *Geophys. Res. Lett.*, 34, 1–6, doi:  
630 10.1029/2007GL029742, 2007.

631 49. Yokota, T., Yoshida, Y., Eguchi, N., Ota, Y., Tanaka, T., Watanabe, H., and  
632 Maksyutov, S.: Global concentrations of CO<sub>2</sub> and CH<sub>4</sub> retrieved from GOSAT: First  
633 preliminary results, *SOLA*, 5, 160–163, doi:10.2151/sola.2009-041, 2009.

634 50. Y. Yoshida, N. Kikuchi, I. Morino, O. Uchino, S. Oshchepkov, A. Brill, T. Saeki,  
635 N. Schutgens, G. C. Toon, D. Wunch, C. M. Roehl, P. O. Wennberg, D. W. T.  
636 Griffith, N. M. Deutscher, T. Warneke, J. Notholt, J. Robinson, V. Sherlock, B.  
637 Connor, M. Rettinger, R. Sussmann, P. Ahonen, P. Heikkinen, E. Kyrö, J.  
638 Mendonca, K. Strong, F. Hase, S. Dohe, and T. Yokota, Improvement of the

639 retrieval algorithm for GOSAT SWIR XCO<sub>2</sub> and XCH<sub>4</sub> and their validation using  
 640 TCCON data, Atmos. Meas. Tech., 6, 1533-1547, doi:10.5194/amt-6-1533-2013,  
 641 2013.

642

643 \*Table 1. Vertical grid levels of the NIES TM model

	H, km	$\sigma=P/P_s$	$\approx\Delta$ , m	$\xi(\sigma-\theta$ grid levels), K	Number of levels
Near-surface layer	0-2	1.0-0.795	250	-	8
Free troposphere	2-12	0.795-0.195	1000	- , 330,350,	10
Upper troposphere and stratosphere	12-40	0.195-0.003	1000 2000	365,380,400,415, 435,455,475,500, 545, 590,665,850, 1325,1710	14
Total levels:					32

644

645 Table 2. Temporal and spatial (horizontal) coverage of HIPPO mission flights.

Missions	Sampling Dates	Vertical Profiles Flown	Flight Path Notes
HIPPO-1	January 8-30, 2009	138	Northern polar flight #1 reached 80 °N, Southern ocean flight reached 67 °S, 175 °W (no return to the Arctic a second time).
HIPPO-2	October 31 to November 22, 2009	148	Northern polar flight #1 reached 80 °N, Southern ocean flight reached 66 °S, and 174 °W, Northern polar flight #2 reached 83 °N.
HIPPO-3	March 24 to April 16, 2010	136	Northern polar flight #1 reached 84.75 °N, Southern ocean flight reached 66.8 °S, 170 °E, Northern polar flight #2 reached 85 °N.

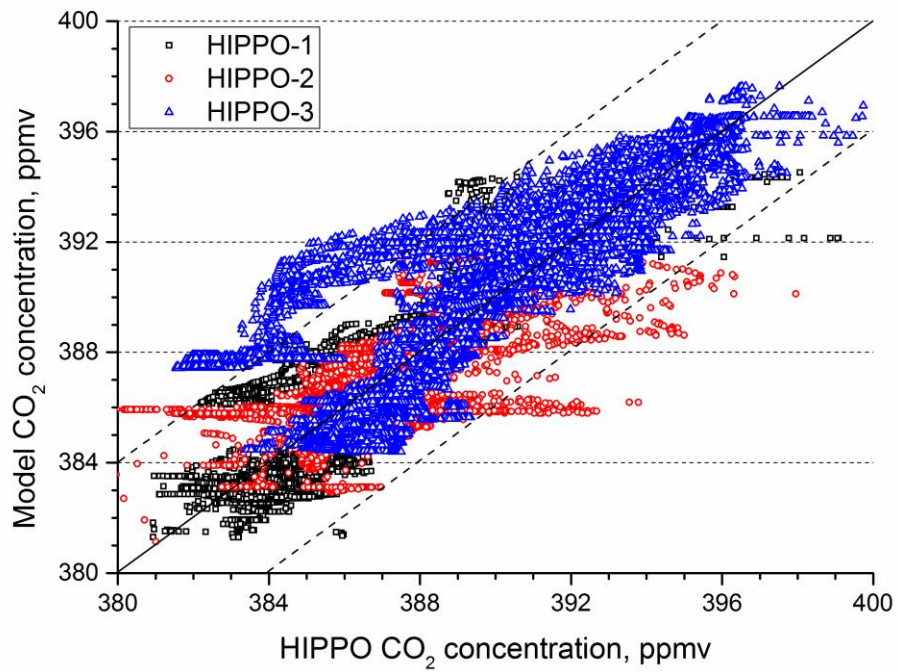
646

647

648

649

\*H, height; P, atmospheric pressure; P<sub>s</sub>, surface atmospheric pressure;  $\Delta$ , vertical integral step;  $\xi$ , the level of the sigma-isentropic grid.



650

651 **Figure 1.** Scatter diagram of modeled and observed CO<sub>2</sub> of HIPPO-1 (black square), 2

652 (red circle), 3 (blue triangle). Dotted lines show a 95% confidence interval

653 of CO<sub>2</sub> concentration.

654

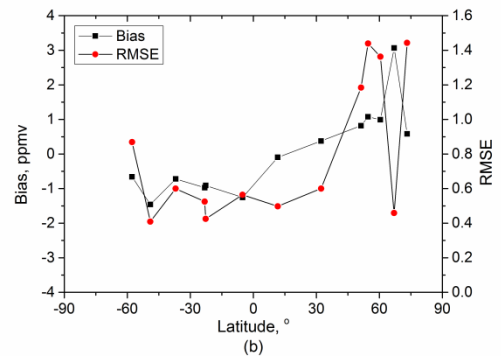
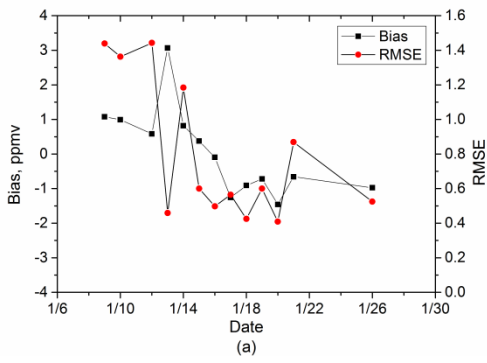
655

656

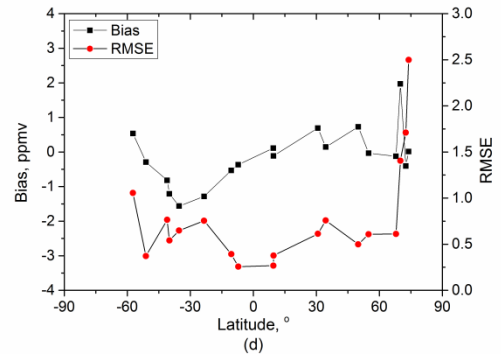
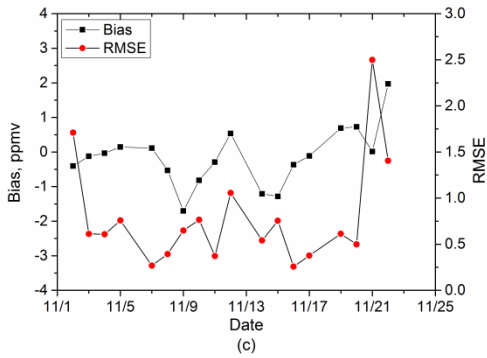
657

658

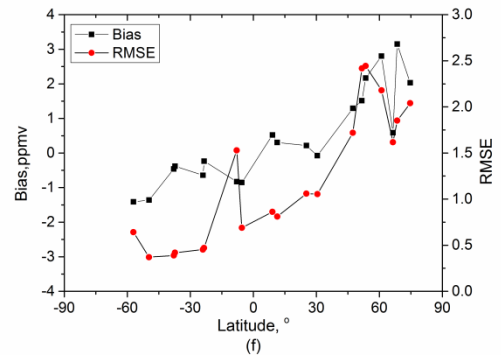
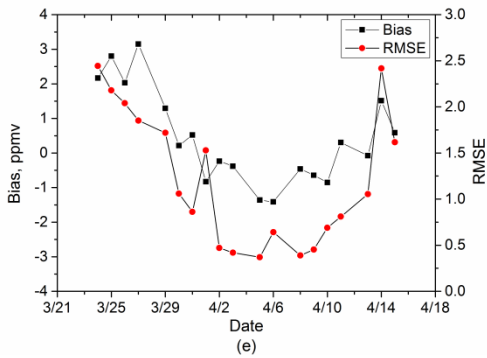
659



660



661



662

663 **Figure 2.** Bias (simulation-observation, black square) and RMSE (red circle) of time-  
 664 ((a) HIPPO-1, (c) HIPPO-2, (e) HIPPO-3) and latitude-varying ((b) HIPPO-  
 665 1, (d) HIPPO-2, (f) HIPPO-3) CO<sub>2</sub> concentration data.

666

667

668

669

670  
671  
672  
673  
674  
675  
676  
677  
678  
679  
680  
681  
682  
683  
684  
685  
686  
687  
688  
689  
690  
691  
692  
693  
694  
695  
696  
697  
698  
699

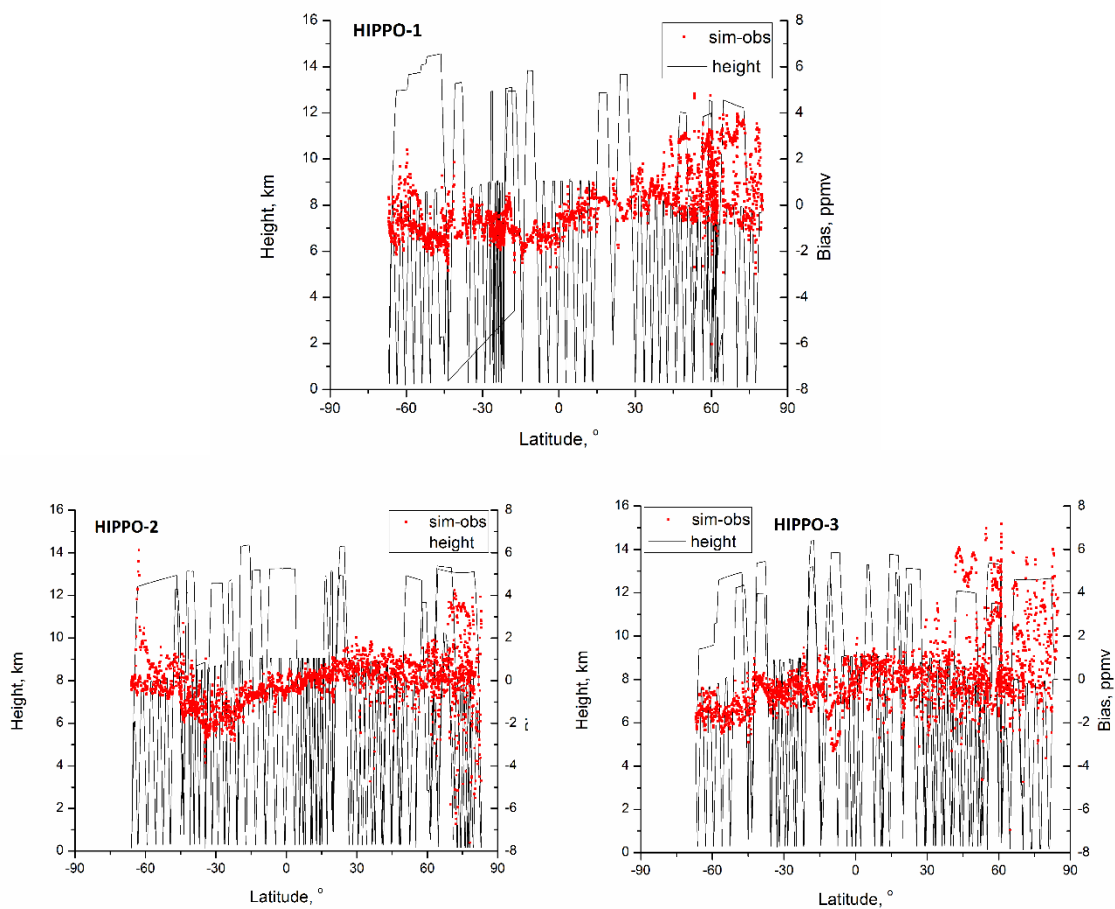
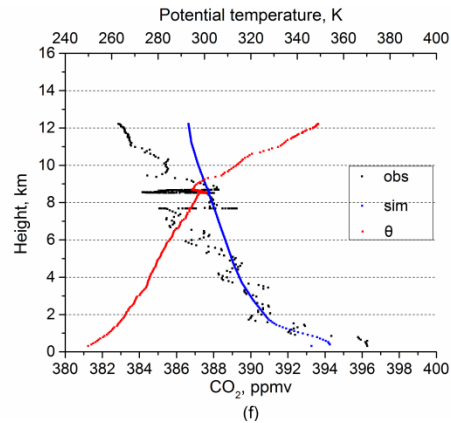
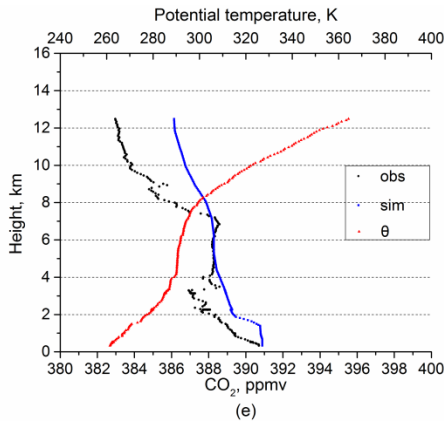
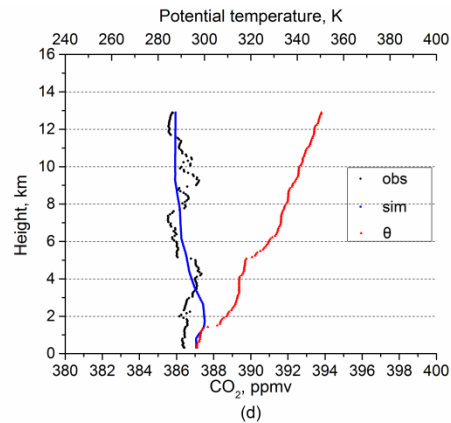
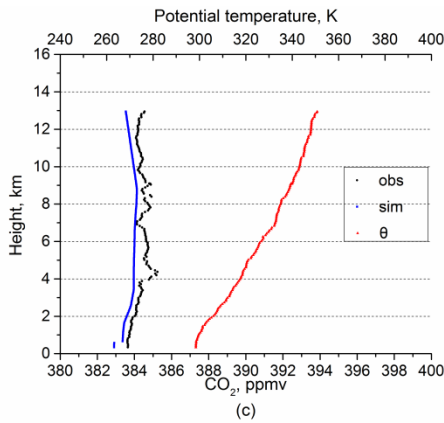
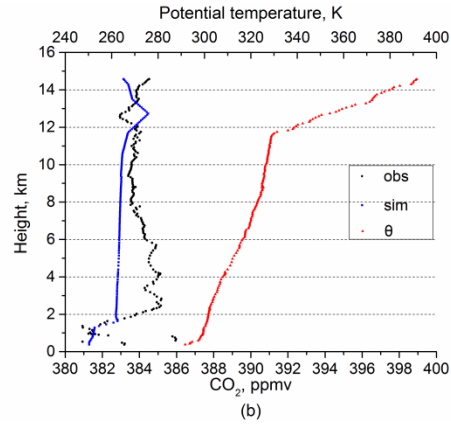
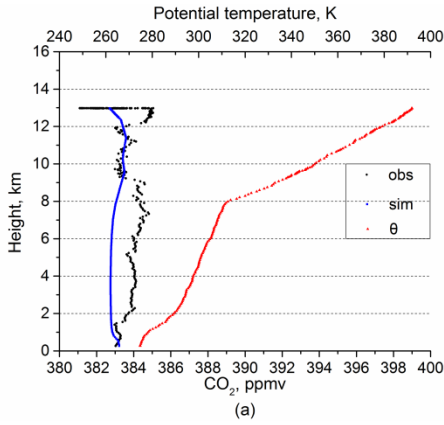


**Figure 3.** Change of flight height and difference between simulation and observation of HIPPO-1, 2, 3 with latitude.



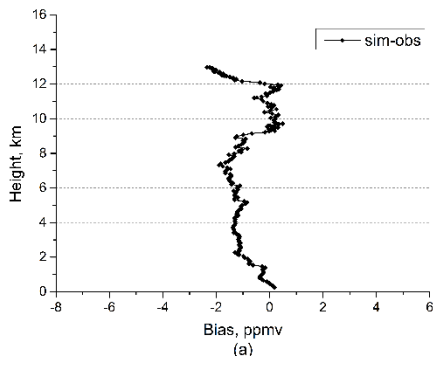
700

701

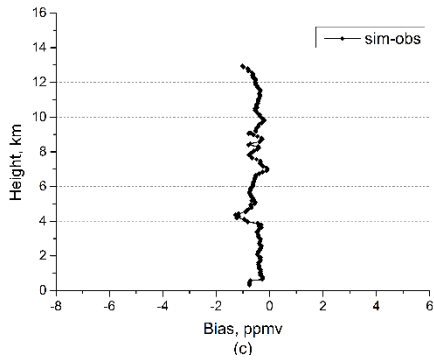
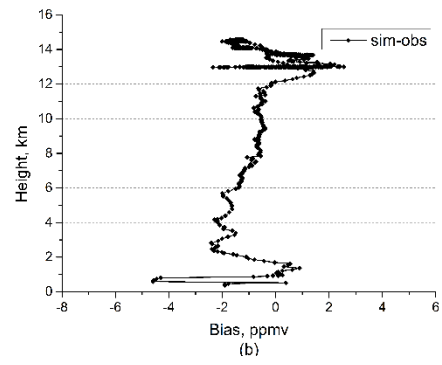
702

703 **Figure 4.** Vertical profiles from near-surface to the LS for HIPPO-1, panels represent  
 704 the vertical profiles of observation (black square), simulation (blue square)  
 705 and potential temperature (red square) in Southern ((a) high-, (b) mid-, (c)  
 706 low- latitude), and Northern Hemisphere ((d) low- , (e) mid-, (f) high-  
 707 latitude).

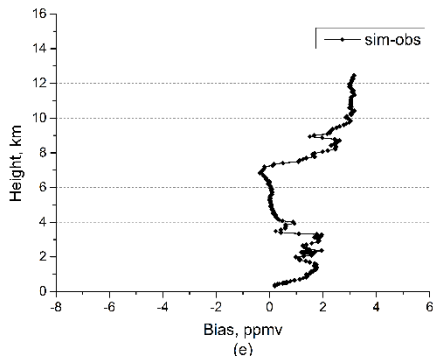
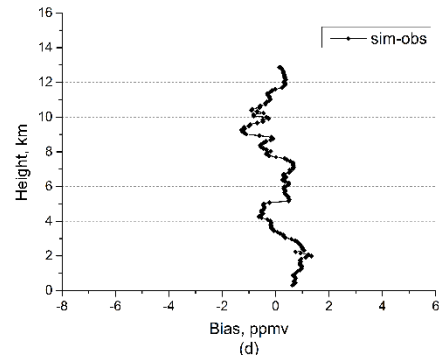
708



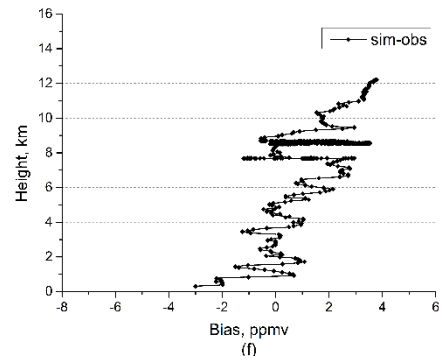
709



710



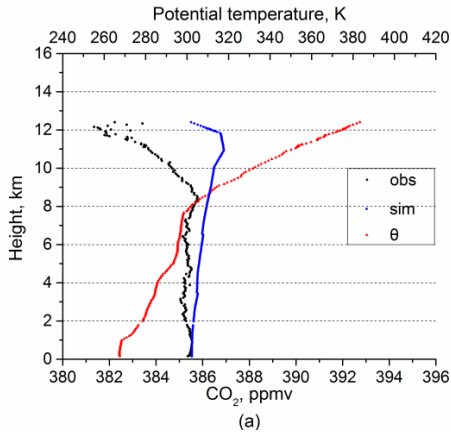
711



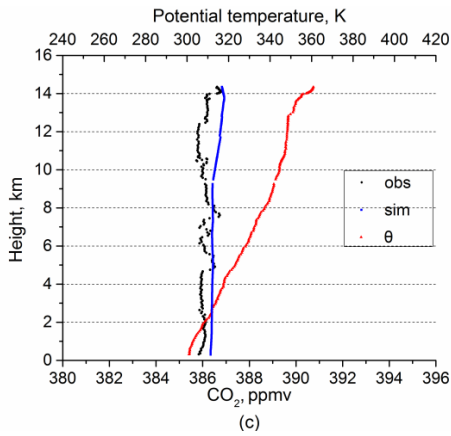
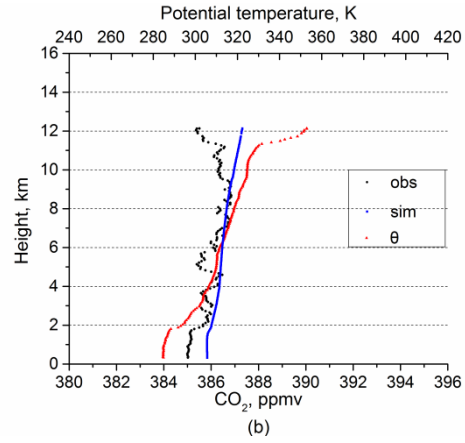
712 **Figure 5.** Biases of simulation minus observation from near-surface to the LS for  
 713 HIPPO-1, panels are corresponding to Figure 4(a)-4(f) respectively.

714

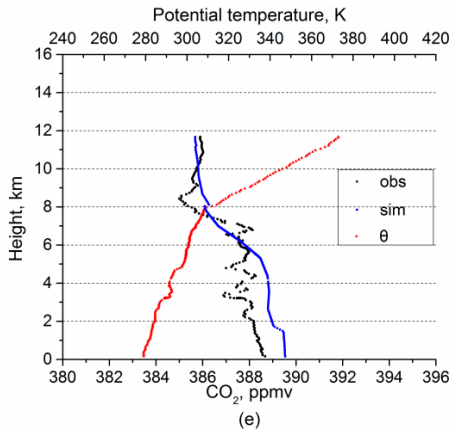
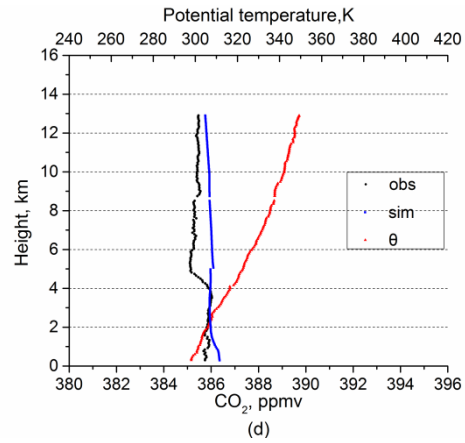
715



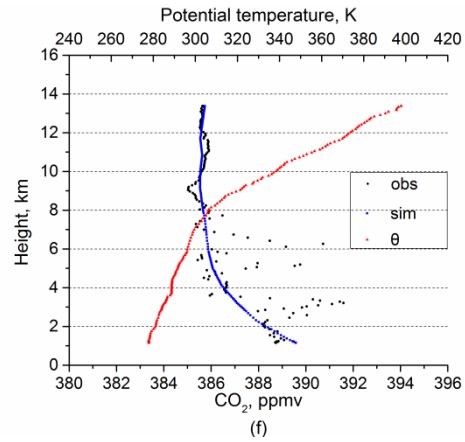
716



717

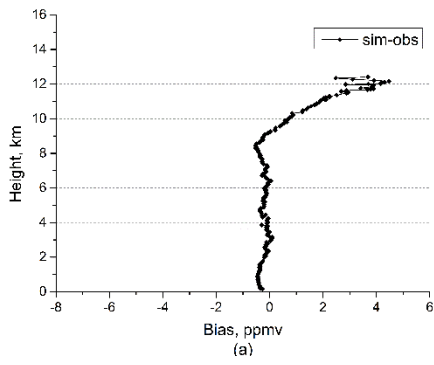


718

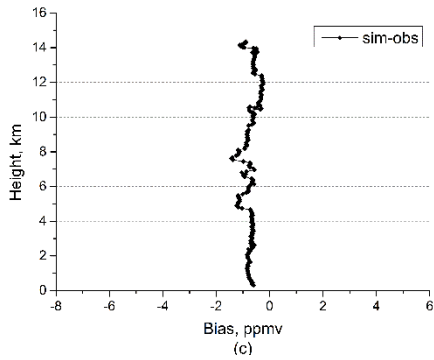
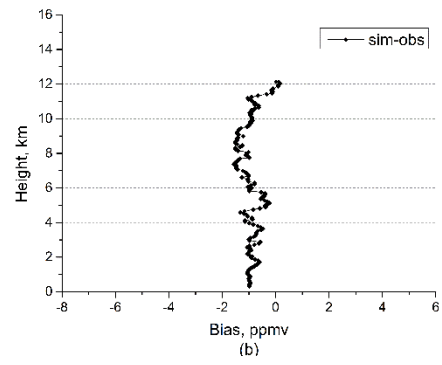


719 **Figure 6.** The vertical profiles from near-surface to the LS for HIPPO-2, panels  
 720 represent the vertical profiles of observation (black square), simulation (blue  
 721 square) and potential temperature (red square) in Southern ((a) high-, (b)  
 722 mid-, (c) low- latitude), and Northern Hemisphere ((d) low-, (e) mid-, (f)  
 723 high- latitude).

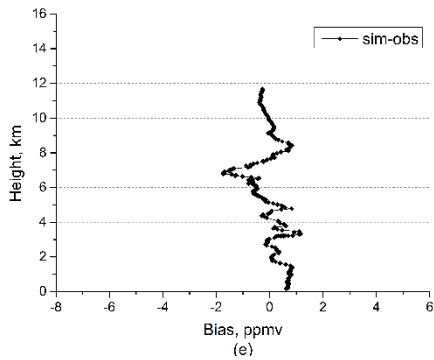
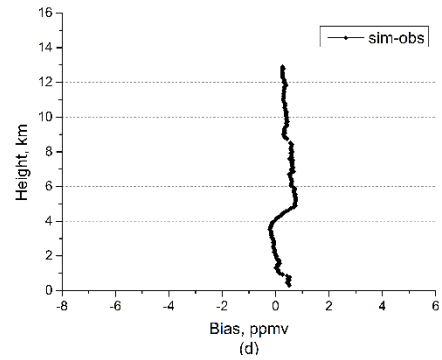
724



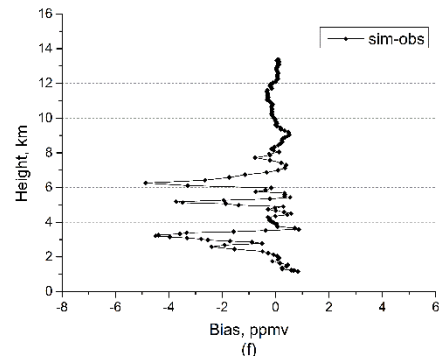
725



726

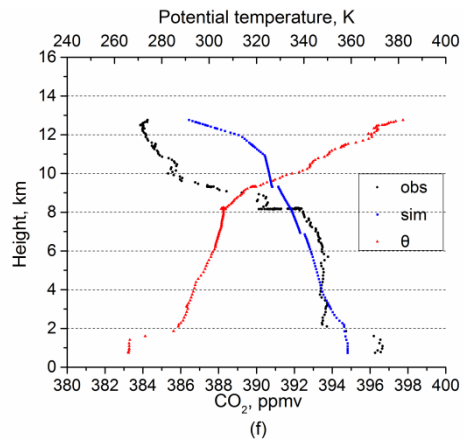
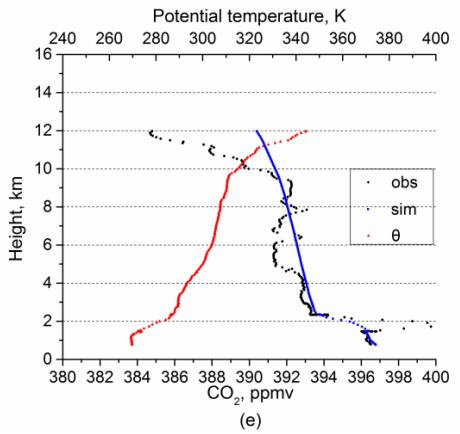
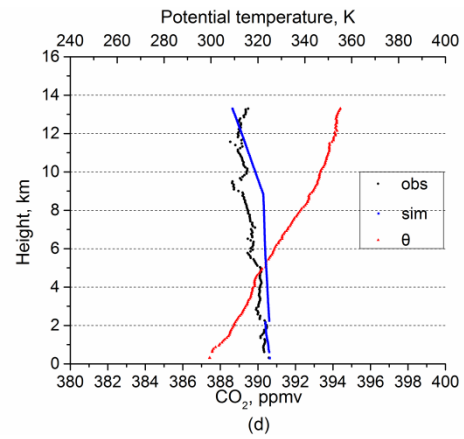
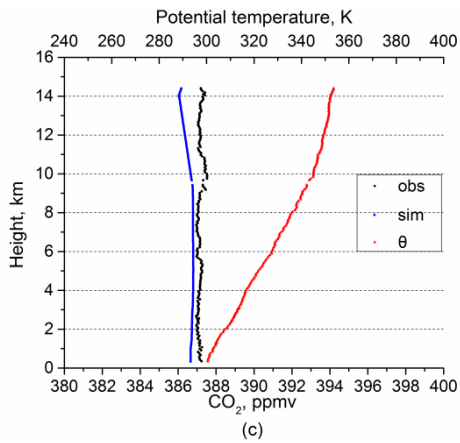
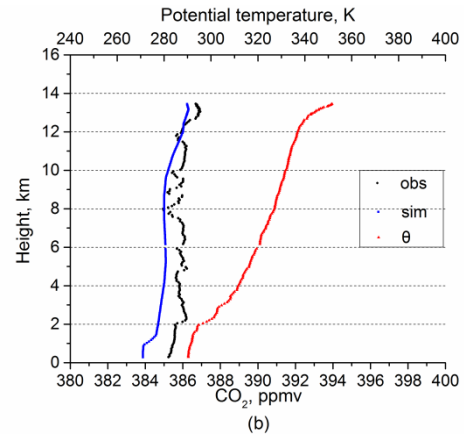
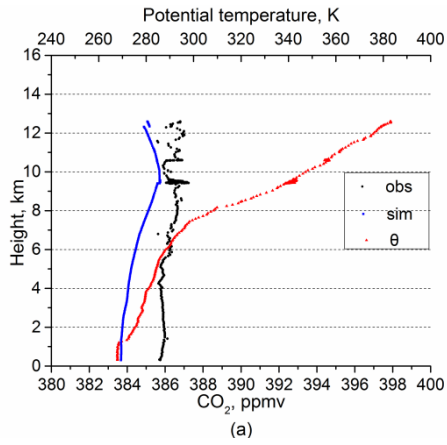


727



728 **Figure 7.** Biases of simulation minus observation from near-surface to the LS for  
 729 HIPPO-2, panels are corresponding to Figure 6(a)-6(f) respectively.

730



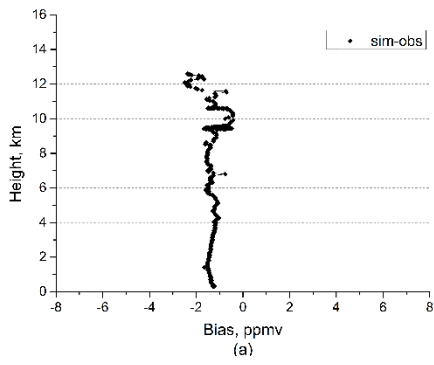
731

732

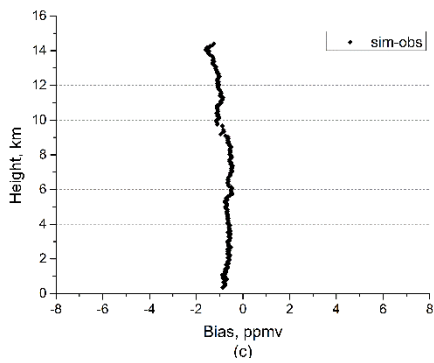
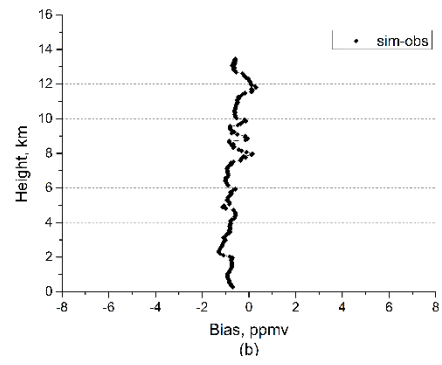
733

734 **Figure 8.** The vertical profiles from near-surface to the LS for HIPPO-3, panels  
 735 represent the vertical profiles of observation (black square), simulation (blue  
 736 square) and potential temperature (red square) in Southern ((a) high-, (b)  
 737 mid-, (c) low- latitude), and Northern Hemisphere ((d) low-, (e) mid-, (f)  
 738 high- latitude).

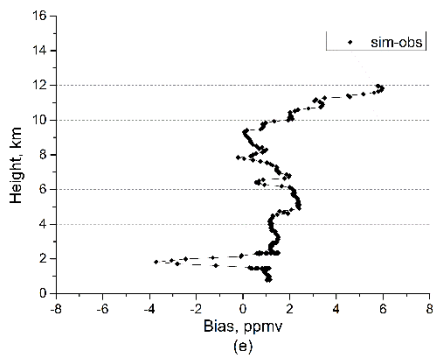
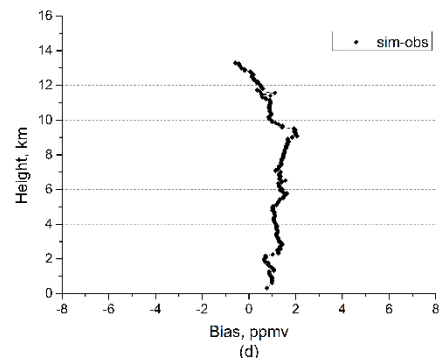
739



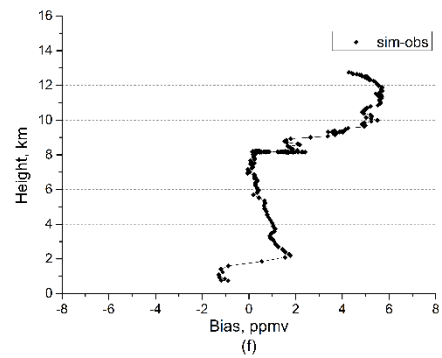
740



741



742



743 **Figure 9.** Biases of simulation minus observation from near-surface to the LS for  
 744 HIPPO-3, panels are corresponding to Figure 8(a)-8(f) respectively.

745